Exploration of crystal strains using coherent x-ray diffraction

2010 New J. Phys. 12 035022

(http://iopscience.iop.org/1367-2630/12/3/035022)

New Journal of Physics
The open-access journal for physics

Exploration of crystal strains using coherent x-ray diffraction

Wonsuk Cha[1], Sanghoon Song[2], Nak Cheon Jeong[3], Ross Harder[4], Kyung Byung Yoon[2,3], Ian K Robinson[5,6] and Hyunjung Kim[1,2,7]

[1] Department of Physics, Sogang University, Seoul 121-742, Korea
[2] Interdisciplinary Program of Integrated Biotechnology, Sogang University, Seoul 121-742, Korea
[3] Department of Chemistry, Sogang University, Seoul 121-742, Korea
[4] Advanced Photon Source, Argonne National Laboratory, Argonne, IL 60439, USA
[5] Department of Physics and Astronomy, University College, London WC1H 0AH, UK
[6] Diamond Light Source, Harwell Campus, Didcot, Oxford OX11 0DE, UK
E-mail: hkim@sogang.ac.kr

New Journal of Physics **12** (2010) 035022 (10pp)
Received 26 October 2009
Published 31 March 2010
Online at http://www.njp.org/
doi:10.1088/1367-2630/12/3/035022

Abstract. We measured coherent x-ray diffraction (CXD) on zeolite micro-crystals in order to gain information on internal density distribution and to learn more about the strain developed during the synthesis and attachment process on the substrate. From the distortion and asymmetry of the diffraction pattern on the (020) Bragg peak, the strain field distribution is estimated. We inverted the diffraction patterns from a less strained crystal to obtain the three-dimensional image of the shape and internal strain fields using the error reduction and hybrid input–output phase retrieval algorithms. We also show a few examples of characteristic distortion modes relevant to CXD of zeolites.

[7] Author to whom any correspondence should be addressed.

Contents

1. Introduction

Templated surfaces open the path to exciting applications of arrays of nano- and micron-sized crystals. Self-organized microcrystals [1] in the form of uniformly aligned and closely packed layers on substrates have potential applications in both bioscience and materials science. Some successful methods have been demonstrated for organizing microcrystals with closely packed mono- and multilayers on glass and other substrates through various well-defined covalent and ionic linkages [2], using zeolite crystals as model microcrystals [3]. Zeolites are a class of crystalline aluminosilicate minerals having pores spaced regularly with the dimension of 0.3–1.5 nm. They have been widely used in industrial applications such as catalysis, ion exchangers and adsorbers [4]. These crystals also have potential applications as nuclear waste scavengers and quantum confinement hosts for semiconductor materials. Most of these applications involve thermal processing for attaching the crystals on the substrate. In that process, the strain can be developed due to different thermal expansion coefficients of zeolites and the substrate material. This can cause grain boundary defects, removal of which is crucial to improve the efficiency in many aspects [5]. In this context, it is important to study how the initial strain appears inside the crystal and how it develops with experimental parameters. However, until now, it has been almost impossible to measure strain distribution inside the crystal *in situ*.

When the crystal is exposed to coherent beams generated from x-ray undulators in third-generation synchrotron sources, scattering from the object will show interference in the diffraction pattern. Fringes from the facets or along the crystal axis are observed in addition to the central conventional Bragg diffraction peak. For the last few years, by inverting such oversampled coherent x-ray diffraction (CXD) patterns using phase retrieval methods, it has been shown that the full three-dimensional (3D) images of the object are successfully obtained [6] as well as internal deformation field distribution [7, 8]. Because the projection of the deformation field to the direction of momentum transfer of the Bragg peak originates from the imaginary component of the complex density distribution, when strain exists one can observe breaking of the symmetry across the Bragg peak.

The opportunity to detect and map out displacement fields in 3D is what makes CXD imaging (CXDI) a particularly exciting method of analysing complex materials such as zeolites. In zeolites and other materials that function on the nanometre length scale, the functionality related to enhanced activity derives from extra degrees of freedom, which are not available to bulk crystalline matter with a fixed lattice. Small crystals can undergo significant deformation without a high cost of free energy. In the case presented in this paper, there are distinct patterns of distortion of the crystals as a whole which may be connected with their activity as catalysts.

2. CXD and strain

A distorted crystal can be represented, in general, as a deformation field acting upon an ideal crystal. The deformation field is a well-defined quantity $\vec{u}(\vec{r})$ representing the vectorial displacement at every point $\vec{r}$ within the crystal. Mechanical distortions, frequently associated with strain fields, tend to be slow-varying, so low-resolution images can often be sufficient to understand their behaviour. It has been shown [8] that the CXD image at the Bragg peak obtained from Fourier inversion of the measurement of a particular reflection $\vec{G}$ in the reciprocal lattice is a complex density distribution in real space. The amplitude of the complex density is proportional to the physical density of the crystal and hence represents the shape. The phase of the complex density $\phi(\vec{r})$ is numerically equal to the projection of the displacement field onto the momentum transfer vector $\vec{Q} \simeq \vec{G}$, providing the master equation $\phi(\vec{r}) = \vec{G} \cdot \vec{u}(\vec{r})$ [8].

Because it is just a projection, the interpretation of the CXDI measurement from a single Bragg peak can be a little limited. However, this has opened up interest in measuring multiple Bragg peaks from the same crystal. Experimental methods for achieving this until now are to use either well-isolated samples or a confocal (3D) alignment microscope [9]. Once three or more non-coplanar measurements are available, it is possible to calculate the full 3D quantity $\vec{u}(\vec{r})$, or the 'D-field' at every point in space [10]. From there, the full strain tensor and local rotations are accessible by spatial differentiation, again as full 3D fields with the same resolution as the image [10]. The single projections are still interesting as they can prove the existence of characteristic distortion modes. In this paper, we will present a few examples of characteristic distortion modes relevant to the zeolite results.

Having said that the first limitation of the complex-density CXDI method (the projection) can be overcome by including additional data, there is a second limitation that still needs to be worked upon. The present-day phasing algorithms (see below), used to assign phases to the measured diffraction amplitudes in reciprocal space, as needed to obtain the image by Fourier transformation, are limited to structures with real-space phases in the range $-\pi/2 < \phi < \pi/2$. This is an experimental finding with our local version of the methods. It is not clear why this should be so, but it may be limited to the situation (applicable in our case) where the real-space amplitude is unconstrained and can drop to zero. When a random starting point is used for phasing, the density can average to zero if the phase is unconstrained, and this may lead to stagnation in the algorithms, usually with the object coming out much too small. Constraining the real-space amplitude is not an option because the shape of the object is usually unknown so zero-valued density points must be allowed within the support, itself a little larger than the object. It is expected that progress will be made in the near future to develop better real-space constraints so that the phase-range limitation can be overcome too. It should also be mentioned that real-space constraints will usually need tuning to the particular sample of interest and that a certain mixture of fitting and refinement might eventually be the best approach.

3. Effects of crystal shape

The first information to be obtained from a CXD pattern concerns the crystal shape. As long as the illuminating beam is coherent across the sample, the fringe spacing of the CXD pattern tells us the dimensions of the sample. This is nicely illustrated for our ZSM-5 crystals because they have simple rectangular prism shapes. Figure 1 shows the calculated 3D CXD patterns for

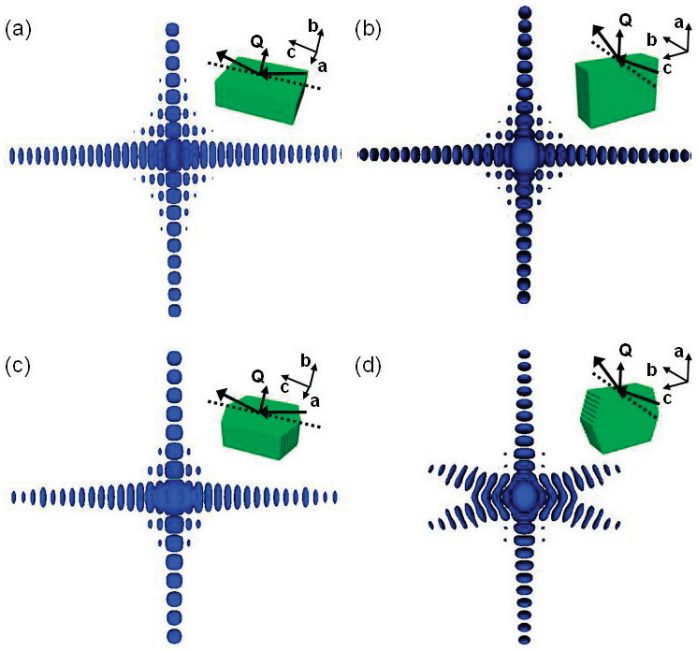

Figure 1. Calculated 3D CXD patterns for a rectangular parallelepiped with the typical ratio between length, width and height of ZSM-5 for the wavevector transfer ($\vec{Q}$) parallel to the $\vec{b}$-axis in (a) and the $\vec{a}$-axis in (b). Those for a hexagonal parallelepiped with an even closer shape with the actual ZSM-5 crystal used in this study are shown for (c) $\vec{Q} \parallel \vec{b}$ (020) and (d) $\vec{Q} \parallel \vec{a}$ (200).

a rectangular parallelepiped with the typical ratio between length, width and height of ZSM-5 for the wavevector transfer ($\vec{Q}$) parallel to the $\vec{b}$-axis in figure 1(a) and the $\vec{a}$-axis in figure 1(b). Those for a hexagonal parallelepiped with an even closer shape with the actual ZSM-5 crystals used in this study are shown for (c) $\vec{Q} \parallel \vec{b}$ (020) and (d) $\vec{Q} \parallel \vec{a}$ (200). If the crystal is ideal, one can observe such diffraction patterns with coherent x-rays and the diffraction pattern is very sensitive to a small modification of the shape. In particular, in figure 1(d), the fringes near the central peak can show a round and connected pattern if they are not well resolved.

4. Strain due to parabolic deformation

We will now consider some of the general trends that are expected in diffraction from simple objects in the presence of strain. A good starting model of one of the zeolite crystals discussed in this paper is a rectangular block of solid (see below). This shape produces three intersecting sets of symmetric fringes, like a 3D slit function, the same around every Bragg peak. The ZSM-5 zeolites are orthorhombic and grow with a significant aspect ratio as plate-like blocks with the thinnest direction along the *b*-axis [11].

The simplest distortion imaginable in such a solid is a beam-bending around the *a*- or *c*-axis. This might be associated with the attachment of the crystal to its substrate, as discussed here, or is possibly relevant to catalysis, as discussed elsewhere [12]. The result is a crystal with a parabolic (dish-shaped) displacement parallel to the *b*-axis, of which the simplest form in the

standard Cartesian coordinates with the origin at the centre of the crystal is

$$\vec{u}(x, y, z) = \alpha x^2 \hat{y},$$

where $\hat{y}$ is a unit vector along the b-axis. If we measure the CXD pattern surrounding one of the $(0k0)$ reflections, the $\vec{Q}$-vector, $\vec{G} = (0, \frac{2\pi}{b}k, 0)$, will be parallel to the displacement and the master equation gives

$$\phi(\vec{r}) = \vec{G} \cdot \vec{u}(\vec{r}) = \frac{2\pi}{b} k\alpha x^2 = \gamma x^2,$$

giving a parabolic phase profile of the complex density in the crystal. The example considered in this paper uses the $k = 2$ (020) reflection of ZSM-5. The values of the coefficients α or γ, which measure the amount of bending, establish two practical limits: the weak phase limit when $|\phi| < \pi/2$ is the regime in which the support-based phasing method works routinely. However, the strong phase limit when $|\phi| > \pi/2$ is extremely likely to occur in practice, especially given that it corresponds to a displacement of the end of the crystal by more than half a lattice constant. This is the regime in which the support-based phasing method does not work at present in our experience and we have to look for new ways to analyse the data.

To see the effect of this simple distortion mode on the expected coherent diffraction pattern, we consider the Fourier transform of a simple one-dimensional block of material of length a, which results in a slit-function diffraction pattern:

$$A_1(q) = \int_{-a/2}^{a/2} \exp(-\mathrm{i}qx)\mathrm{d}x = \frac{2}{q} \sin\left(\frac{qa}{2}\right),$$

where the symbol q is used for the local momentum–transfer displacement from the Bragg peak at $\vec{q} = \vec{Q} - \vec{G}$. For simplicity, the density of the crystal has been set to unity and the cross-sectional pre-factor has been omitted. When the distortion is included, we have the Fourier transform of the complex density,

$$A_2(q) = \int_{-a/2}^{a/2} \exp(\mathrm{i}\phi(x)) \exp(-\mathrm{i}qx)\, \mathrm{d}x = \int_{-a/2}^{a/2} \exp(\mathrm{i}\gamma x^2) \exp(-\mathrm{i}qx)\, \mathrm{d}x.$$

This form is immediately recognizable as the Fresnel integral. The result is exact in both the weak and strong phase limits although, as we shall see below, the form of the function changes significantly. It is easily generalized to 3D. This demonstrates the important point that the far-field diffraction pattern of a simply strained crystal is the same as two other cases: (i) an unstrained crystal measured under plane wave illumination in the 'near field' when the detector is placed closer than the Fresnel distance a^2/λ or (ii) an unstrained crystal measured in the 'far' field under curved-wave illumination from an ideal focusing system. This geometry has been proposed under the name of 'Keyhole Imaging' as a way of solving the phase problem [13]. An object of real density (or any non-refractive object measured in the forward scattering direction) will be distinct from its complex-conjugate 'twin' when imaged using a curved beam; this removes one of the most serious symmetries that can cause phasing algorithms to stagnate.

To illustrate the effect on the diffraction patterns directly, in figure 2 we have calculated some simulated 3D objects with parabolic phase distributions in the upper panel. The calculations are done with an FFT on a $128 \times 128 \times 128$ array on a cube-shaped object of $40 \times 24 \times 12$ grid points. The introduced parabolic phase functions are shown on a colour wheel with green representing $\phi = 0$, blue $\phi = -\pi$ and red $\phi = \pi$. The amplitudes of the calculated diffraction patterns (in the lower panel) are shown on a standard rainbow colour scale.

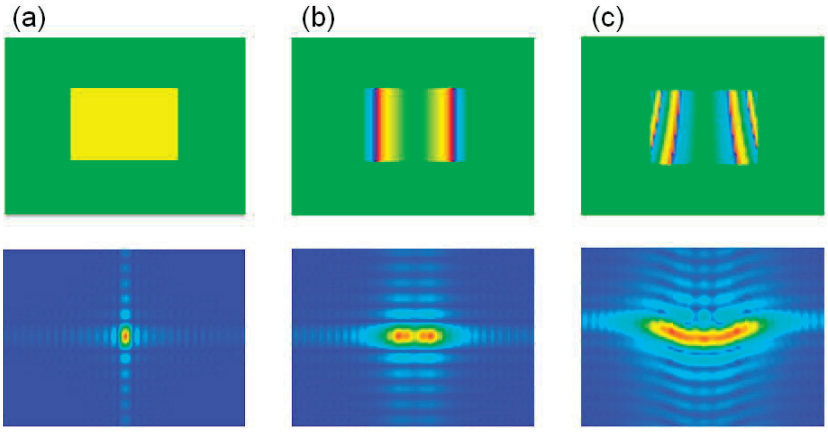

Figure 2. Simulated 3D rectangular parallelepiped objects with parabolic phase distributions (upper panel) and the corresponding calculated diffraction patterns (lower level). The calculations are done with a fast Fourier transform (FFT) on a $128 \times 128 \times 128$ array on a cube-shaped object of $40 \times 24 \times 12$ grid points. The introduced parabolic phase functions are shown on a colour wheel with green representing $\phi = 0$, blue $\phi = -\pi$ and red $\phi = \pi$. Note that several phase wraps appear in the plots. The amplitudes of the calculated diffraction patterns are shown on a standard rainbow colour scale. In (a), the pattern was generated for the unstrained, i.e. with uniform phase throughout the object.

In figure 2(a), the pattern was generated for the unstrained, i.e. with uniform phase throughout the object. (In this case, the yellow colour does not have meaning for a particular value.) In figure 2, the amount of phase curvature, set by parameter γ, increases from left to right. Figure 2(a) has $\gamma = 0$ and is the far-field diffraction pattern of a rectangular object, just as in figure 1. Figure 2(b) has about 2π of phase curvature at the two ends of the block, resulting in a single wrap of the phase in the plot. This gives a broadened centre to the diffraction pattern with two peaks instead of one, resembling two slit diffraction patterns side by side. Figure 2(c) has two full wraps of phase between the centre and each end. This results in further broadening of the calculated Bragg peak, which now has about four maxima. In addition, a ramping of the curvature parameter γ has been included, which has the effect of bending the extended shape of the diffraction centre. We will see below that these peak shapes occur experimentally for the zeolites.

5. CXD measurements of ZSM-5

Among the many different types of zeolites, ZSM-5 was used in this study. The detailed synthesis process can be found elsewhere [14]. In order to attach ZSM-5 crystals onto the Si substrate, a colloidal solution was prepared by dispersion of ZSM-5 crystals into a solution of polyethylene imine (PEI) dissolved in ethanol. The Si substrate was cleaned by piranha solution for 30 min. The ZSM-5 dispersed colloidal solution was spun-cast on the Si substrate. Subsequently, organic components of PEI were eliminated by calcination at 450 °C for 15 h. While they were calcined, the chemical bonds of Si–O–Si were formed at the contacts of the zeolites and the Si substrate.

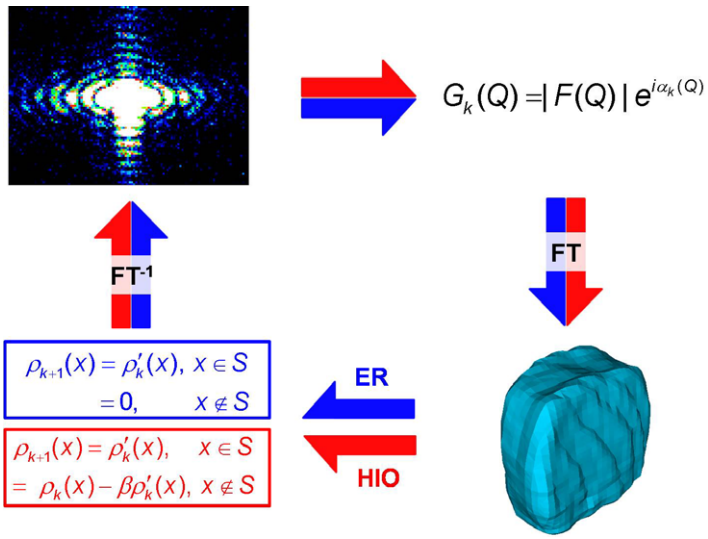

Figure 3. Schematic diagram of phase retrieval algorithm combined with ER and HIO using CXD. See the text for details.

The CXD measurements were carried out at the beamline 34-ID-C at the Advanced Photon Source, USA. Coherent x-rays with an energy of 9 keV were employed and the beam size was $20 \times 25\ \mu\text{m}^2$. The typical sample size was $1.9 \times 0.8 \times 2.7\ \mu\text{m}^3$ and lattice constants of ZSM-5 are 20.02, 19.90 and 13.38 Å along the a-, b- and c-axis, respectively. Most of the crystals have favoured orientation of (020) when they are lying down on the substrate. A charge-coupled device (CCD)-based position-sensitive detector with 22.5 μm pixels was used for taking 3D diffraction data. The (020) Bragg peak was typically collected with steps of 0.005° of the sample tilt angle, ϕ, and with 61 frames in total at a sample–detector distance of 2.9 m.

Combinations of error reduction (ER) and hybrid input–output (HIO) phase retrieval algorithms [15] were applied, in this study, to the data. A phase variation in the range $\pm\pi/2$ was used as an additional real-space constraint. Figure 3 shows a schematic diagram of the phasing algorithm. In the algorithm, in order to obtain the image and phase information from the 3D CXD data, satisfying oversampling conditions, one can start Fourier transform first with a given random phase (α_k) and the amplitude (square root of intensity, $F = \sqrt{I}$) from the measurement at a given wavevector transfer (Q) and then apply alternating cycles of ER and the HIO algorithm. If point x lies within the finite support (S), which is the real-space constraint, the input $\rho(x)$ is set to the output $\rho'(x)$. Otherwise it is set to zero in ER, or else to $\rho(x) - \beta\rho'(x)$ in HIO. In HIO, the only free parameter β is typically set between 0.7 and 0.9. The value satisfying the direct space constraints of the algorithm at the kth iteration is ρ_k. The iterative calculation is typically performed in 120 iterations of ER, 300 of HIO and 120 of ER in sequence. The fractional error was less than 0.035 on average in the diffraction amplitude. Better results were obtained from the ER–HIO–ER calculation than from only ER or HIO alone.

Figure 4(a) shows a CXD pattern taken at the centre from (020) of ZSM-5 at room temperature in vacuum, and the CXD pattern shows asymmetry in both the horizontal and vertical directions, implying that strain has been developed. The reconstructed image with respect to the direction of the x-ray beam in figure 4(b) shows the entire shape of the reconstructed image being in close resemblance with SEM pictures of ZSM-5. The size obtained

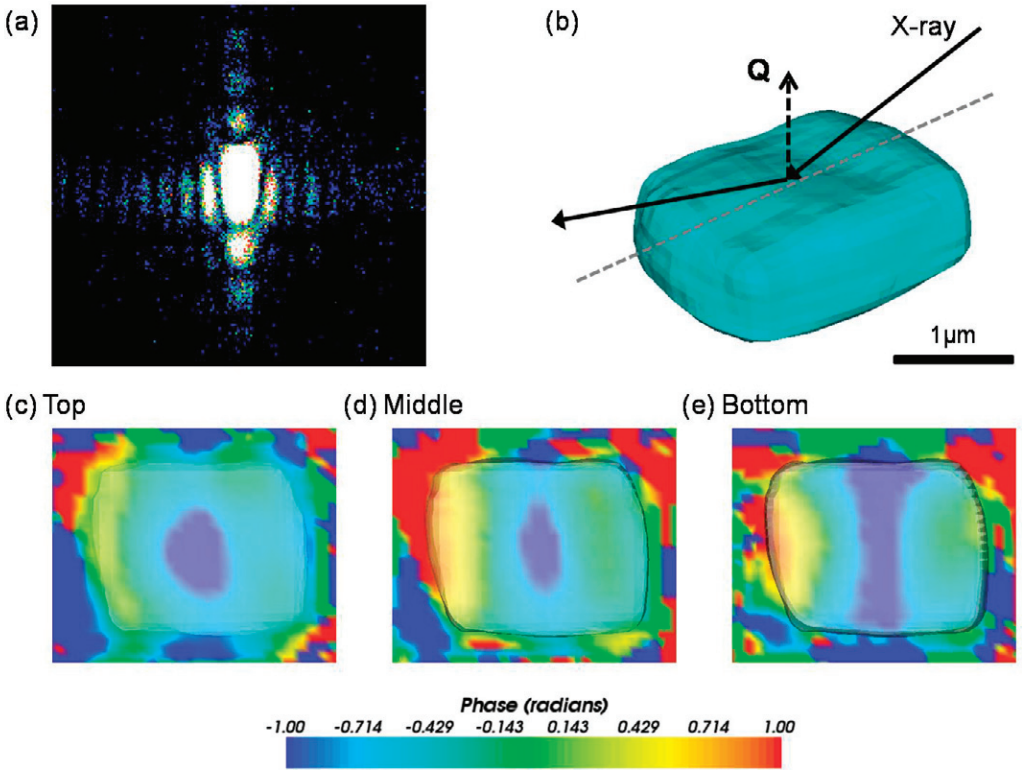

Figure 4. (a) CXD pattern for ZSM-5 along (020). (b) A reconstructed image with respect to the direction of the x-ray beam. The phases cross sectioned (c) near the top surface, (d) at the centre and (e) near the bottom. The phase with a colour scale ranging from blue (−1 rad) to red (+1 rad) is interpreted in quantity as a projection onto the Q-vector of the deformation of the crystal.

was $1.9 \times 0.9 \times 2.5\ \mu m^3$. The support used was ± 12, ± 8 and ± 12 and the constraint was $\pm \pi/2$. The inversion of the diffraction data as a function of wavevector transfer to a complex density function also yields a real-space phase value for every point in space. The phases cross-sectioned near the top surface, at the centre and near the bottom are shown in figures 4(c)–(e). As discussed earlier in this paper, the phase ranging from blue (−1 rad) to red (+1 rad) in colour scale is interpreted in quantity as a projection onto the Q-vector of the deformation of the crystal [8]. A phase of +1 is in accord with a shift of $\pi/2$ of (020) lattice spacing, or 0.3 nm. It is interesting to observe that the edges of the crystal have more positive phase than the middle. This might be due to the different gradient in thermal expansion between the zeolites and Si substrate [16]. However, the strain was still small enough to be able to get images from the diffraction pattern. Note that even though the phases outside the crystal are shown, the amplitudes outside the crystal are minimal in magnitude.

Figure 5 shows (020) diffraction patterns from a selection of ZSM-5 crystals with apparently different amounts of strain. The size of the crystals was the same as that of the crystal shown in figure 4 and was measured at 50 °C. The simple pattern of figure 4(a) was relatively uncommon; the most common pattern was similar to figure 5(b). It can be seen that the horizontal extension of the Bragg peak resembles the patterns predicted in figure 2, with figure 2(b) approximating figure 5(b). Figure 5(b) has three columns of fringes as if the crystal is

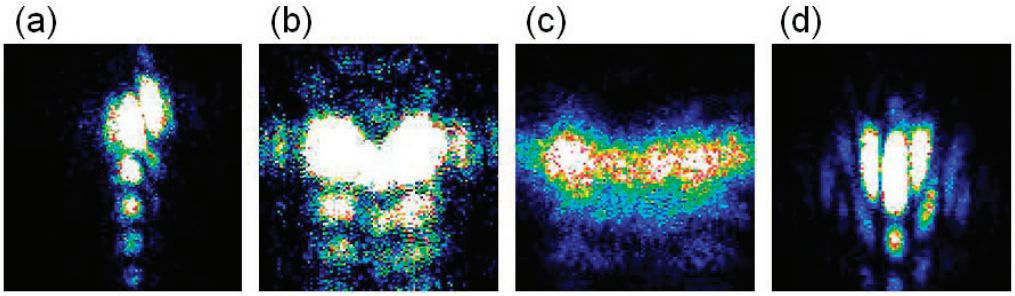

Figure 5. Some of the coherent diffraction patterns from (020) ZSM-5 zeolites with a highly strained lattice. The crystals shown in (a) and (d) were found to be rotated (about the normal) at different angles with respect to the direction of x-rays.

split into three sections; these correspond to the peaks of the Fresnel integral seen in figure 2(b), which are also seen to form columns of fringes. Figure 5(c) is even more strained, with about four peaks on a bent distribution; this resembles figure 2(c), where the bending was simulated by varying the phase curvature across the crystal.

Until now, it has not been possible to phase the diffraction patterns in figure 5. To develop a general method of doing so, it may be useful to start with simple modelling, as in figure 2. It should, in principle, be possible to estimate the degree of parabolic distortion across the crystal by simple fringe counting. The bending effect can be simulated too. It may then be possible to constrain the real-space phase in ER and HIO to $\pm\pi/2$ around the fit value and thereby eventually succeed in phasing the data.

Our results show that the deformation field in a microcrystal can be detected by CXD with high sensitivity by non-destructive and *in situ* measurements. With higher flux and larger coherent fraction from the next-generation sources like the x-ray free electron laser (XFEL) and energy recovery linac (ERL), the techniques with coherent x-rays such as the CXD technique will be more easily explored.

Acknowledgments

This work was supported by Basic Science Research Program through the National Research Foundation of Korea (NRF) funded by the Ministry of Education, Science and Technology (nos 2009-0053982 and R15-2008-006-01001-0), Seoul Research and Business Development Program (10816), Sogang University Research Grant (2009) and an ERC FP7 Advanced Grant. Use of the Advanced Photon Source was supported by the US Department of Energy, Office of Science, Office of Basic Energy Science, under contract no. DE-AC02-06CH11357.

References

[1] Clark T D, Tien J, Duffy D C, Paul K E and Whitesides G M 2001 *J. Am. Chem. Soc.* **123** 7677
[2] Kulak A, Lee Y-J, Park Y S and Yoon K B 2000 *Angew. Chem. Int. Ed.* **39** 950
[3] Lee J S, Lee Y-J, Lee Tae E, Park Y S and Yoon K B 2003 *Science* **301** 818
[4] Davis M E 2002 *Nature* **417** 813

[5] Choi J, Jeong H-K, Snyder M A, Stoeger J A, Masel R I and Tsapatsis M 2009 *Science* **325** 590
[6] Williams G J, Pfeifer M A, Vartanyants I A and Robinson I K 2003 *Phys. Rev. Lett.* **90** 175501
[7] Pfeifer M A, Williams G J, Vartanyants I A, Harder R and Robinson I K 2006 *Nature* **442** 63
[8] Robinson I K and Harder R 2009 *Nat. Mater.* **8** 291
[9] Beitra L, Watari M, Matsuura T, Shimamoto N, Harder R and Robinson I unpublished
[10] Newton M C, Leake S J, Harder R and Robinson I K 2010 *Nat. Mater.* **9** 120
[11] Kokotalio G T, Lawton S L, Olson D H and Meier W M 1978 *Nature* **272** 437
[12] Cha W, Song S, Jeong N C, Harder R, Yoon K B, Robinson I K and Kim H unpublished
[13] Abbey B, Nugent K A, Williams G J, Clark J N, Peele A G, Pfeifer M A, De Jonge M and McNulty I 2008 *Nat. Phys.* **4** 394
[14] Lermer H, Draeger M, Steffen J and Unger K K 1985 *Zeolites* **5** 131
[15] Fienup J R 1982 *Appl. Opt.* **21** 2758
[16] Marinkovic B A, Jardim P M, Rizzo F, Saavedra A, Lau L Y and Suard E 2008 *Micropor. Mesopor. Mater.* **111** 110